# Influence of annealing atmosphere on the structural phase changes and optical properties of $TiO_2$ nanoparticles

*Bhagya* Uthaman[1*], *Anjali* Krishnan[1], *Sona* S Prabha[1], and *V. R.* Akshay[2†]

[1]Department of Physics, Fatima Mata National College (Autonomous), Kollam, Kerala, India-691001
[2]M. Dasan Institute of Technology, Ulliyeri PO, Kozhikode, Kerala, India-673323

**Abstract.** In the present work, structural and optical behaviour of sol-gel synthesized $TiO_2$ and Nitrogen doped $TiO_2$ (N-doped $TiO_2$) nanoparticles calcined under air and vacuum atmosphere have been analysed. N-doped $TiO_2$ samples were synthesized by adding ammonia as nitrogen source and as reducing agent. The molar concentration of Ammonia was fixed at 1 M and 2 M respectively. The incorporation of nitrogen into the $TiO_2$ samples was verified using X-ray photoelectron spectroscopy (XPS). X-ray diffraction (XRD) was used to examine the structural characteristics of air and vacuum-annealed samples, and Scherrer equation was used to determine the average crystallite size. Raman analysis was carried out to understand all the major modes of vibration in the annealed samples. UV-visible spectroscopy was carried to analyse the effect of different atmospheres on the band gap of the samples. Photoluminescence studies were used to understand the presence of defect states in the sample.

## 1. Introduction

$TiO_2$ is an indirect wide band gap semiconductor used in numerous applications such as photocatalysis [1, 2], biosensors [3], solar cells [4], pigments [2], antibacterial agent [5], batteries [6], supercapacitors [7], etc. The low cost, non-toxicity, abundance, good chemical stability, excellent oxidation capacity makes them an excellent candidate for research [8]. Anatase $TiO_2$ is widely exploited as an excellent candidate for photocatalytic applications. However, its use as a photocatalyst is restricted to the near UV region due to the large intrinsic bandgap ~3.2 eV [9]. To tune the bandgap to the visible region, several methods have been suggested with include the doping of $TiO_2$ with d-block transition elements such as Fe, Cu, and non-metals such as C, N, Boron, etc. [10]. Several reports on N-doping using ammonia gas, urea, etc. has been reported. N-doping was found to lower the band gap via the introduction of N-doping centers and a reduced electron-hole recombination rate [10-12].

* Corresponding author: bhagyautham13@gmail.com, bhagya@fmnc.ac.in
† Corresponding author: vijayrajakshay@gmail.com

In this study, we have used a simple sol-gel route to synthesise N-$TiO_2$ nanoparticles. Ammonia was used as the nitrogen (N) source. It has been suggested that N- doping could be a useful way to introduce defects into the system and hence could be used to tune properties such as photocatalytic activity [10-12]. In addition, defects could also be introduced by annealing $TiO_2$ in a controlled environment [13]. Herein, we report the combined effect of N-doping and vacuum annealing on the introduction of defects and tuning the band gap of anatase $TiO_2$.

## 2. Experimental details

Pristine $TiO_2$ nanoparticles have been synthesised using titanium isopropoxide, isopropanol and deionised water as starting materials. Initially stoichiometric amounts of isopropanol and deionised water were mixed and heated. Then titanium isopropoxide was slowly added dropwise with continuous stirring. The precursor solution was then heated for 3 hours. Finally, a white residue was obtained, which was ground using agate mortar and pestle to obtain the precursor. To prepare nitrogen doped $TiO_2$ (N-$TiO_2$), a strong reducing agent ammonia was introduced in the solution during the synthesis procedure. Here we have used 1M and 2M solution of ammonia to prepare N-$TiO_2$ samples. These prepared precursor samples were then divided into two batches. The first batch was calcined at 400 ºC for 4 hours in a muffle furnace in air to get Pristine $TiO_2$ labelled as TP0, and 1M and 2M N-$TiO_2$ samples represented as TP1 and TP2 respectively. The second batch was calcined under vacuum atmosphere in a tubular furnace at the same temperature and were labelled as TPV0, TPV1 and TPV2 respectively. Powder samples were subjected to X-ray photoelectron spectroscopy (XPS) utilising Al-Kα X-rays with an energy of 1486.6 eV using a Thermo Scientific ESCALAB Xi+ equipment. Initially, a wide scan was recorded to ensure that the sample surface was free of any foreign materials. The elemental oxidation states were further confirmed using the high-resolution XPS scan of Ti 2p, N 1s and O 1s regions. The XPS spectrum was fitted using XPSPEAKfit 4.1 after subtracting the background using Shirley method. The C 1s peak at 284.8 eV was used to calibrate the measured binding energy. The X-ray diffraction pattern of each sample was recorded using a PHILIPS X'PERT PRO powder diffractometer employing Cu-Kα (λ=1.54060 Å) radiation. The diffraction profiles were scanned over the range 20˚ to 80˚ with a step of 0.017º. Raman spectra in the range 100-800 $cm^{-1}$ were recorded using a Horiba LabRAM HR Evolution spectrometer equipped with lasers of wavelength 532 and 785 nm. UV-visible absorbance spectra of $TiO_2$ were recorded using Jasco V650 spectrophotometer in the range 200 to 900 nm and band gap was estimated using Tauc's Plot. An Edinburgh FLS 1000 spectrometer, with an excitation wavelength of 325 nm from a 150 W xenon lamp was used to analyse photoluminescence (PL).

## 3. Results and discussion

### *3.1.* XPS Analysis

XPS, a surface-sensitive method, yields insights into the chemical environment of the ionic species located on the sample surface. As a representative of the series, the survey spectra of TP0, TP1 and TPV1 are shown in Fig.1(a-c). High-resolution spectra of selected samples were taken and are shown in Fig.2 (a-f) respectively. The Ti 2p spectra of TP0 sample has only a single peak corresponding to $Ti^{4+}$ as shown in Fig.2(a). Interestingly, TP1 sample exhibit a multiple oxidation state of $Ti^{4+}$and $Ti^{3+}$. The formation of $Ti^{3+}$ is ascribed to the introduction of N into the $TiO_2$ lattice. The O 1s high resolution spectra of TP1 is deconvoluted into three peaks corresponding to lattice oxygen of $TiO_2$ ($O_L$), oxygen vacancy

($O_V$) and hydroxyl group (-OH) oxygen, respectively and is presented in Fig 2(c). The band gap narrowing discussed in the next section could be attributed to the presence of mixed oxidation states. Due to introduction of N into the lattice, $O_V$ have been created due to the formation of $Ti^{3+}$, which introduced intermediate energy levels in the bandgap, contributing to the band gap narrowing. Hence, in TP1 sample, both $O_V$ and $Ti^{3+}$ contribute to band gap reduction via creating additional energy levels. N 1s binding energy peak at 399.54 eV for TP1 sample confirms the introduction of N into the lattice as shown in Fig 2(d). The peak at 403.37 eV of N 1s can be represented as satellite peak. The increase in lattice parameter could be ascribed to the introduction of $O_V$ into the lattice upon introducing a strong reducing agent such as ammonia.

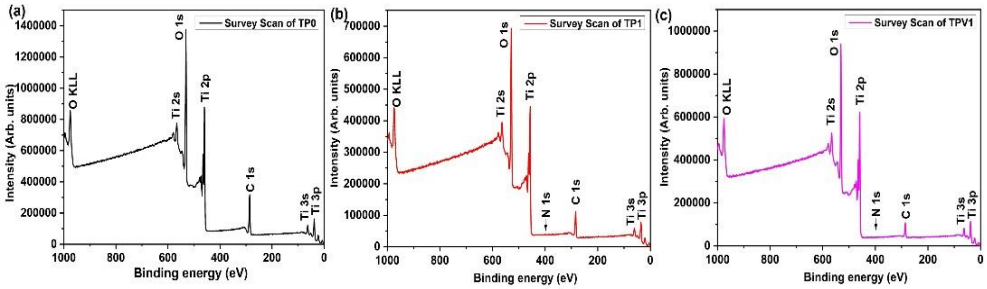


**Fig. 1.** Survey scans of (a) TP0, (b) TP1 and (c) TPV1

Upon vacuum annealing, a broadening of Ti 2p peak could be seen in TPV1 sample as shown in Fig 2(e). Upon deconvolution of peaks, it could be seen that the amount of $Ti^{3+}$ has increased in comparison to TP1 sample. Also, in the O 1s spectra, the presence of $O_V$ has increased as shown in Fig 2(f) as compared to TP1 sample. The increase in $O_V$ and $Ti^{3+}$ is due to the combined effect of N-doping and vacuum annealing. Thus, it could be affirmed with previous reports that N-doping and vacuum annealing creates defects into the system and could influence the structural and optical behaviour of $TiO_2$ [13].

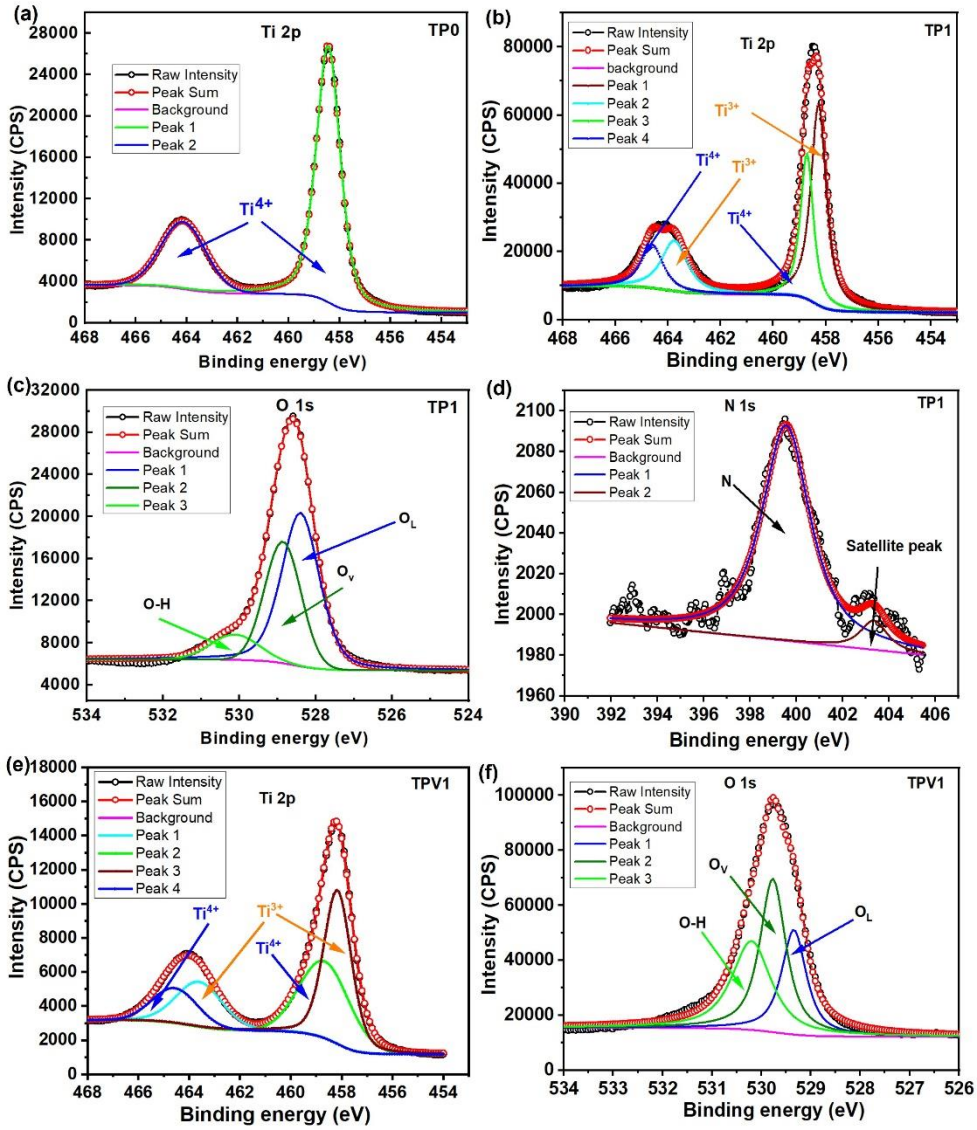


**Fig. 2.** High Resolution scan of (a) Ti 2p in TP0, (b) Ti 2p in TP1, (c) O 1s in TP1, (d) N 1s in TP1, (e) Ti 2p in TPV1 and (f) O 1s in TPV1.

## *3.2.* Structural studies

### *3.2.1. XRD Analysis*

Fig. 3 (a and b) shows the indexed XRD patterns of air and vacuum annealed samples respectively. All the samples crystallise into the anatase phase of $TiO_2$ with tetragonal structure having space group I41/amd and all the peaks could be well indexed with ICDD 78-2486. In TP0, the peak at 31.5° corresponds to the (110) plane of the rutile phase. It could be seen that with the increase in the molar concentration of Ammonia, the rutile phase has been suppressed and only anatase phase is seen in TP1 and TP2. A similar trend is also observed for vacuum annealed samples TPV0, TPV1 and TPV2 as seen in Fig 3(b).

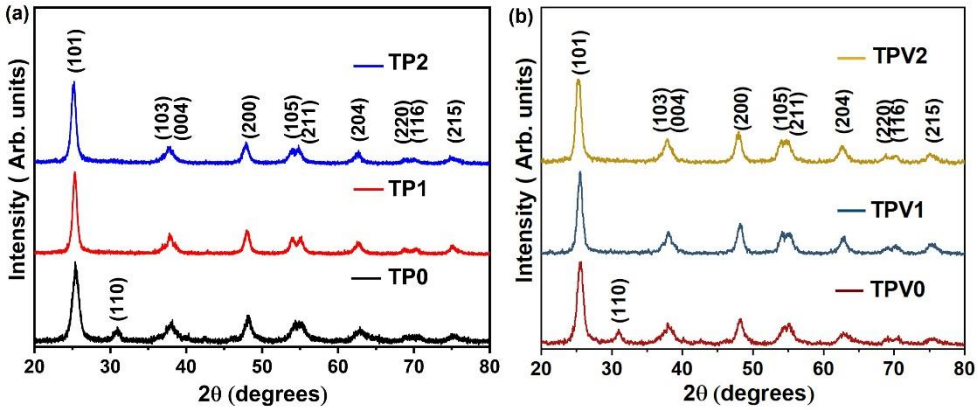


**Fig.3.** XRD patterns of (a) Air annealed samples (b) Vacuum annealed samples

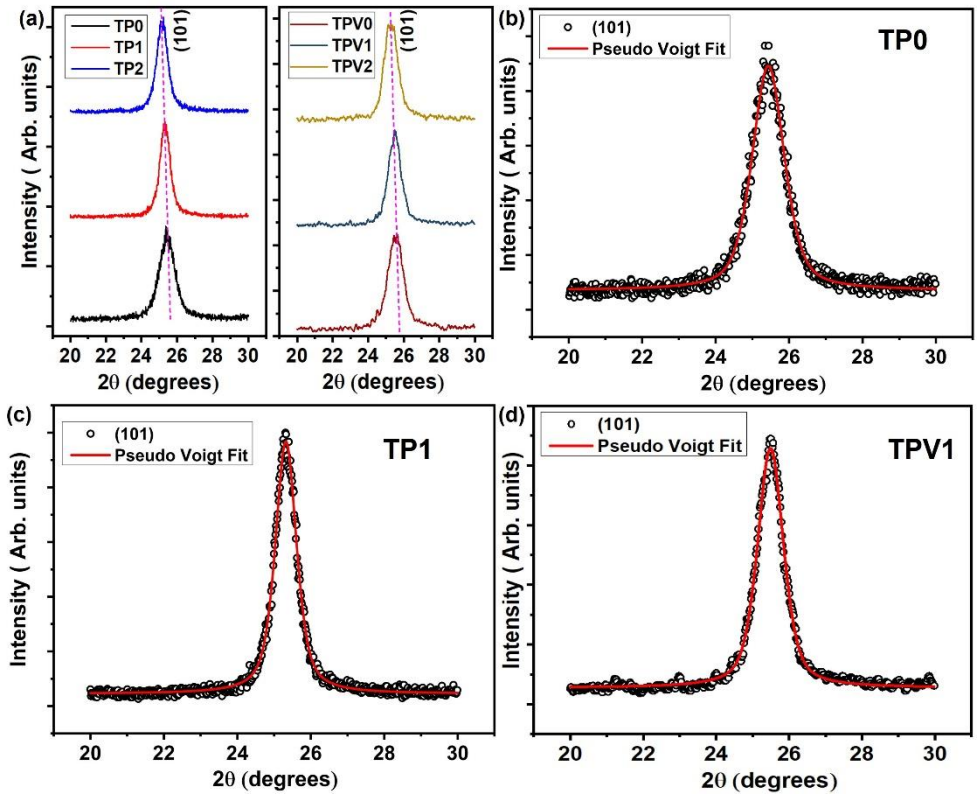


**Fig. 4** (a) Peak shift corresponding to air and vacuum annealed samples (b-d) Curve fitting of (101) peak of TP0, TP1 and TPV1.

Fig. 4(a) shows the peak shift for (101) plane of air and vacuum annealed samples. The N-$TiO_2$ samples TP1 and TP2, exhibit a blue shift compared to the pristine sample TP0. As the doping percentage increases, Bragg angle θ become smaller. Consequently, when sinθ decreases, the interplanar spacing, d increases. The increase in d spacing affirms the incorporation of N into the lattice, thereby leading to increase in lattice parameters. In vaccum annealed samples, a similar blue shift corresponding to air annealed samples has been

observed as seen in Fig 4 (a). Fig 4(b-d) shows the curve fitting to the (101) peak of TP0, TP1 and TPV1 respectively. However, with vacuum annealing, broadening of peaks has been observed which is attributed to a smaller crystallite size. The crystallite size has been estimated from Scherrer equation

$$t = \frac{K\lambda}{\beta \cos\theta} \qquad (1)$$

where t is the size of a crystallite, K is a constant that depends on crystallite size and is taken as 0.9, λ is the wavelength of X-rays used (1.5060 Å), θ is the Bragg diffraction angle and β is termed as the full width at half maximum (FWHM). The parameters obtained from the curve fitting of the XRD peaks is tabulated in Table 1. The values of lattice parameters estimated and the crystallite size deduced from Scherrer equation has been tabulated in Tables 2 and 3 respectively.

**Table 1.** Interplanar spacing for air and vacuum annealed samples

| Sample | Plane (h k l) | 2θ (in degrees) | d- spacing (Å) | Sample | Plane (h k l) | 2θ (in degrees) | d- spacing (Å) |
|---|---|---|---|---|---|---|---|
| **TP0** | (101) | 25.4337 | 3.5010 | **TPV0** | (101) | 25.4124 | 3.5030 |
| | (200) | 48.1872 | 1.8878 | | (200) | 48.0192 | 1.8932 |
| | (105) | 53.9857 | 1.6980 | | (105) | 53.7320 | 1.7046 |
| | (211) | 55.0679 | 1.6672 | | (211) | 55.0324 | 1.6677 |
| **TP1** | (101) | 25.3226 | 3.5161 | **TPV1** | (101) | 25.3102 | 3.5172 |
| | (200) | 48.0325 | 1.8935 | | (200) | 48.0008 | 1.8938 |
| | (105) | 53.9845 | 1.6980 | | (105) | 53.7256 | 1.7048 |
| | (211) | 55.0628 | 1.6672 | | (211) | 55.0314 | 1.6674 |
| **TP2** | (101) | 25.1637 | 3.5380 | **TPV2** | (101) | 25.0567 | 3.5511 |
| | (200) | 47.8744 | 1.8994 | | (200) | 47.5678 | 1.9101 |
| | (105) | 53.8721 | 1.7013 | | (105) | 53.5673 | 1.7094 |
| | (211) | 54.8488 | 1.6733 | | (211) | 54.5463 | 1.6810 |

**Table 2.** Lattice parameters estimated for air and vacuum annealed samples

| Sample | a (Å) | c (Å) | Sample | a (Å) | c (Å) |
|---|---|---|---|---|---|
| **TP0** | 3.7757 | 9.3500 | **TPV0** | 3.7762 | 9.3502 |
| **TP1** | 3.7871 | 9.4649 | **TPV1** | 3.7885 | 9.4656 |
| **TP2** | 3.7989 | 9.7138 | **TPV2** | 3.7992 | 9.7140 |

**Table 3.** Determination of average crystallite size using Scherrer equation for air and vacuum annealed samples

| Sample | Plane | β | θ (degree) | Crystallite size (nm) | Average crystallite size (nm) |
|---|---|---|---|---|---|
| **TP0** | (101) | 1.0443 | 12.7169 | 7.8026 | 9.4495 |
| | (200) | 1.0499 | 24.094 | 8.2915 | |
| | (105) | 0.7686 | 26.9926 | 11.6038 | |
| | (211) | 0.8874 | 27.5319 | 10.0991 | |
| **TP1** | (101) | 0.6875 | 12.6613 | 11.8498 | 11.2235 |
| | (200) | 0.8078 | 24.0163 | 10.7717 | |
| | (105) | 0.7459 | 26.9923 | 11.9578 | |
| | (211) | 0.8687 | 27.5314 | 10.3164 | |
| **TP2** | (101) | 0.7476 | 12.5818 | 10.8935 | 11.4354 |
| | (200) | 0.8103 | 23.9372 | 10.7312 | |
| | (105) | 0.7183 | 26.9361 | 12.4105 | |
| | (211) | 0.7648 | 27.4244 | 11.7070 | |
| **TPV0** | (101) | 1.0643 | 12.7062 | 7.6554 | 9.3057 |
| | (200) | 1.0549 | 24.0096 | 8.2476 | |
| | (105) | 0.786 | 26.866 | 11.3345 | |
| | (211) | 0.8974 | 27.5162 | 9.9855 | |
| **TPV1** | (101) | 0.6905 | 12.6551 | 11.7973 | 10.9984 |
| | (200) | 0.8182 | 24.0004 | 10.6328 | |
| | (105) | 0.791 | 26.8628 | 11.2626 | |
| | (211) | 0.8699 | 27.5157 | 10.3011 | |
| **TPV2** | (101) | 0.7546 | 12.52835 | 10.7898 | 11.3972 |
| | (200) | 0.8298 | 23.7839 | 10.4666 | |
| | (105) | 0.7203 | 26.78365 | 12.3594 | |
| | (211) | 0.7468 | 27.27315 | 11.9728 | |

### *3.2.2. Raman Analysis*

Raman spectroscopy is an extremely powerful tool to understand the material's phase, surface disorder and the presence of deformities or defects. The synthesised samples show six active Raman modes corresponding to anatase $TiO_2$. The modes have been labelled as $E_g$ (1), $B_{1g}$ (1), $A_{1g}$, $E_g$ (2), $B_{1g}$ (2) and $E_g$ (3). The $E_g$, $A_{1g}$ and $B_{1g}$ modes involve symmetric

stretching, anti-symmetric stretching and symmetric bending vibrations of O-Ti-O bonds respectively. The Raman spectra of air and vacuum annealed samples are shown in Fig. 5 (a) and 5(b) respectively. The inset of 5(a) and 5(b) shows the magnified spectra of $E_g(1)$ peak. The $E_g(1)$ mode of air annealed samples exhibit a blue shift together with peak broadening as seen in the inset of Fig. 5 (a). This could be ascribed to the nonstochiometry in $TiO_2$ due to the introduction of $O_V$ due to the formation of $Ti^{3+}$ when N is introduced into the $TiO_2$ lattice [13]. On the contrary, in vaccum annealed samples, no evident peak shift is observed, however broadening of peaks could be seen which is associated with the introduction of $O_V$ both due to N doping and vacuum annealing.

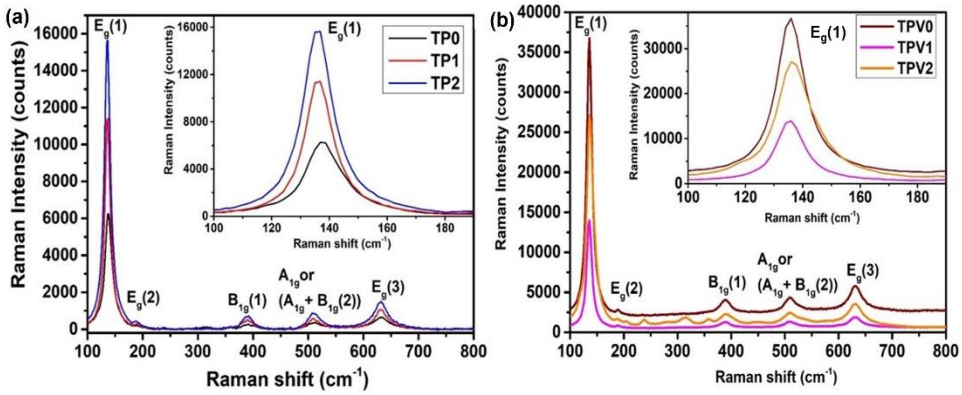


**Fig. 5.** Raman spectra of (a) Air annealed (b) Vacuum annealed $TiO_2$ samples. Insets show the shift and broadening of $E_g(1)$ mode.

## *3.3.* Optical studies

### *3.3.1. UV-visible Analysis*

To understand the influence of N-doping and different annealing environment on the band gap of $TiO_2$ samples, absorbance spectra in the range 200-900 nm were recorded and the band gap was estimated using Tauc's plot. Fig 6 (a) and 6 (c) show the absorbance spectra of air and vacuum annealed samples respectively. The N-doped and vacuum annealed samples display a sharp rise in absorption at ~ 300-400 nm which is associated with the inherent bandgap absorption of anatase $TiO_2$ in the UV region. The reported band gap of anatase $TiO_2$ is 3.2 eV [14-15]. The band gap of air and vacuum annealed samples have been estimated using Tauc's plot and the band gaps of the TP0, TP1 and TP2 were estimated to be 3.32, 3.27 and 3.25 eV, respectively. In vacuum annealed samples, a further decrease in band gap was observed and they were estimated to be 3.30, 3.23 and 3.21 eV for TPV0, TPV1 and TPV2 respectively. The reduction in band gap is due to the formation of $O_V$ both due to N-doping and vacuum annealing leading to the formation of $Ti^{3+}$ centers, which in turn, form additional donor levels in the lattice of $TiO_2$ [13]. Both $O_V$ and $Ti^{3+}$ generate new energy levels below the conduction band (CB) favouring band gap narrowing.

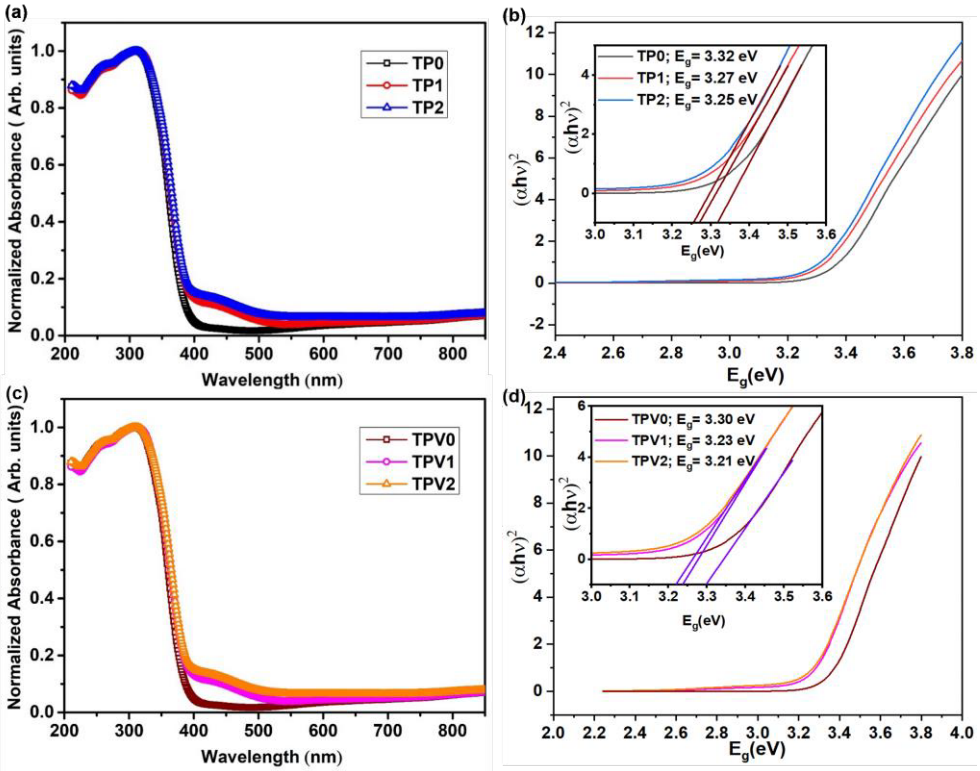


**Fig. 6.** Normalized Absorbance spectra of (a) Air annealed (c) Vacuum annealed $TiO_2$ samples, Tauc's plots for (b) Air annealed samples (d) Vacuum annealed samples

### *3.3.2. Photoluminescence studies*

PL spectrum of the air annealed and vacuum annealed samples recorded at an excitation wavelength of 325 nm is displayed in Fig. 7(a) and 7(b) respectively. They provide insights into the radiative and non-radiative recombination pathways of photoexcited electrons via distinct trap levels such as shallow traps (ST) and deep traps (DT). The N-doped air and vacuum annealed samples show sharp emission peaks with slight variations in the PL intensity. The PL spectra shows transitions in the range 350 to 700 nm. The UV emission peak ~ 380 nm corresponds to the inter-band transition of electrons from CB minimum to valence band, positioned at distinct k-points in Brillouin zone [16]. Furthermore, the PL emission peaks are closely linked to the radiative decay of self-trapped excitons (STE) and ST and DT centers connected to oxygen defect centres. Transitions involving ST are responsible for emission peaks in the range 405–468 nm (3.06–2.65 eV), while transitions involving DT are responsible for those in the region 480–590 nm (2.58–2.10 eV). ST levels include STE, $O_V$, and impurities [15] and act as radiative recombination centers, whereas the DT levels, are specifically formed from oxygen defects and serve as non-radiative recombination sites. The emissions at 363 and 381 nm correspond to STE. STE's are formed when an electron localized at a lattice site traps a hole and gives rise to UV emission. The presence of $O_V$ in the ST and DT levels in the band gap of $TiO_2$ result in oxygen defect related emissions [17]. ST involve $Ti^{3+}$ states located just below the CB and correspond to blue-green emission. DT levels are associated with oxygen defects associated with $O_V$ and N centers. In air annealed samples, the presence of $Ti^{3+}$ and $O_V$ are less compared to vacuum

annealed samples. Hence, in vacuum annealed samples, more DT centers have been created that act as non-radiative recombination sites resulting in quenching of PL signals. The schematic illustration of excitation and emission process in $TiO_2$ is shown in Fig 8.

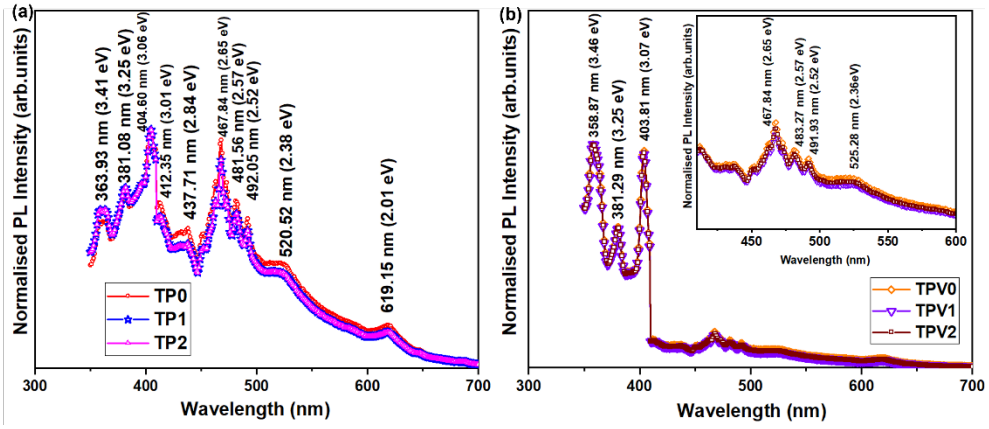


**Fig.7.** PL spectra of (a) Air annealed and (b) Vacuum annealed $TiO_2$ samples

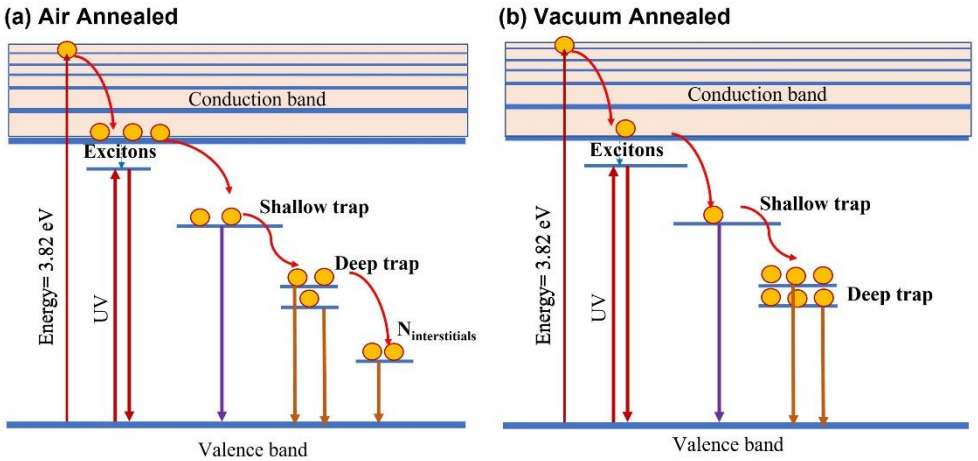


**Fig.8.** Schematic representation of plausible PL emission mechanism in (a) Air annealed and (b) Vacuum annealed $TiO_2$ samples

## 4. Conclusion

In the present work, pristine $TiO_2$ and N-doped $TiO_2$ nano samples have been synthesized through sol-gel route. The samples have been annealed in air and vacuum atmospherse. The XPS analysis of air annealed sample confirms that N has been incorporated into the lattice of $TiO_2$. Air annealed sample shows both $Ti^{3+}$ and $Ti^{4+}$ states, while with vacuum annealing, the percentage of $Ti^{3+}$ and $O_V$ increases. The XRD pattern of the samples were analysed and the phase purity, peak shift, lattice constant and average crystallite size were studied. The average crystallite size was found to be in the range of 9-11 nm for air annealed samples and was found to decrease with vacuum annealing. The UV-spectral studies of the samples reveal narrowing of band gap with increase in the concentration of ammonia. The band gap further reduces with vacuum annealing which is attributed to the formation of $O_V$ and $Ti^{3+}$ centers.

Quenching of PL emission peaks has been observed with vacuum annealing which is attributed to the creation of non-radiative deep trap levels in comparison to shallow trap levels. Hence, it could be seen that N-doped $TiO_2$ samples could be used for further applications such as photocatalysis, dilute magnetic semiconductors, etc.

## Acknowledgements

The facilities of CLIF, Kariavattom are deeply acknowledged. BU, AK, SSP acknowledges KSCSTE via Letter no. 01086/SPS 65/2021/KSCSTE and Fatima Mata National College (Autonomous), Kollam via Letter no FC/E3/SM12/2022 for financial support.

## References

1. S.A. Al-Zahrani, K. Umar, S.A. Tweib, J.A.M. Rashd, S.K. Afridi, S.A. Bhawani, A. Al Otaibi, N. Masood, D. Mansour, A. Khan, M. Ayyar, Biomass-mediated synthesis of ZnO and ZnO/GO for the decolorization of Methylene Blue under visible light source, Catalysts **13(2)**, 409 (2023) https://doi.org/10.3390/catal13020409
2. B.A. van Driel, P.J. Kooyman, K.J. van den Berg, A. Schmidt-Ott, J. Dik, A quick assessment of the photocatalytic activity of $TiO_2$ pigments — From lab to conservation studio!, Microchemical Journal **126**, 162–171(2016) https://doi.org/10.1016/j.microc.2015.11.048
3. G. Mele, R. D. Sole and X. Lü, Titanium Dioxide ($Tio_2$) and Its Applications, (Metal Oxides, 2021, Pages 527-581)
4. A. A. Hendi, M. M. Alanazi, W. Alharbi, T. Ali, M. A. Awad, K. M. Ortashi, H. Aldosari, F. S. Alfaifi, R. Qindeel, G. Naz, T. H. Alsheddi, M. Ben Rabha, M.F. Boujmil, M. Saadoun, B. Bessaïs, Journal of King Saud University – Science **35,** 102555 (2023) https://doi.org/10.1016/j.jksus.2023.102555
5. K. S. Khashan, G. M. Sulaiman, F. A. Abdulameer, S. Albukhaty, M. A. Ibrahem, T. Al-Muhimeed and A.A. AlObaid, Antibacterial Activity of $TiO_2$ Nanoparticles Prepared by One-Step Laser Ablation in Liquid, Appl. Sci., **11(10)**, 4623 (2021) https://doi.org/10.3390/app11104623
6. H. Shi, C. Shi, Z. Jia, L. Zhang, H. Wang and J. Chen, Titanium dioxide-based anode materials for lithium-ion batteries: structure and synthesis, RSC Adv., **12**, 33641 (2022) https://doi.org/10.1039/D2RA05442F
7. R. Lakra, R. Kumar, S. kumar, D.Thatoi , A. Soam, Synthesis of $TiO_2$ nanoparticles as electrodes for supercapacitor, Materials today proceedings, Volume 74, Part 4, 2023, Pages 863-866 10.1016/j.matpr.2022.11.271
8. W. Mekprasart, T. Khumtong, J. Rattanarak, W. Techitdheera and W. Pecharapa, Effect of Nitrogen Doping on Optical and Photocatalytic Properties of $TiO_2$ Thin Film Prepared by Spin Coating Process, Energy Procedia **34**, 746 – 750 (2013) https://doi.org/10.1016/j.egypro.2013.06.809
9. S.B. Deshmukh, K.H. Deshmukh, M. L. Mane, D.V. Mane, Effect of Nitrogen doping on structural and optical properties of $TiO_2$ nanoparticles, Macomol. Symp. **400**, 2100071 (2021) 10.1002/masy.202100071
10. P. H. Le, L.T. Hieu, T-N. Lam, N.T.N. Hang, N. V. Truong, L. T. C. Tuyen, P.T. Phong, J. Leu, Enhanced photocatalytic performance of Nitrogen doped $TiO_2$ Nanotube arrays using a simple annealing process, Micromachines, **9,** 618 (2018) https://doi.org/10.3390/mi9120618

11. S. Du, J. Lian, F. Zhang, Visible Light-responsive N-doped $TiO_2$ Photocatalysis: Synthesis, Characterizations and Applications. Transactions of Tianjin University, **28**, 33–52 (2022) https://doi.org/10.1007/s12209-021-00303-w
12. K. Kusumandari, O.D. Wijayanti, Y. Iriani, T. E. Saraswati and B. Purnama, The Impact of nitrogen doping variations on the effectiveness of $TiO_2$ as a photocatalyst for methylene blue degradation, Journal of Physics: Conference Series 2945, 012052 (2025) 10.1088/1742-6596/2945/1/012052
13. V.R. Akshay, B. Arun, M. Mukesh, Anupama Chanda, M. Vasundhara, Tailoring the NIR range optical absorption, band-gap narrowing and ferromagnetic response in defect modulated $TiO_2$ nanocrystals by varying the annealing conditions, Vacuum, 184, 109955 (2021) 10.1016/j.vacuum.2020.109955
14. S.M. Gupta, M. Tripathi, A review of $TiO_2$ nanoparticles, Chin. Sci. Bull. **56**, 1639–1657 (2011)
15. B. Choudhury, A. Choudhury, Oxygen defect dependent variation of band gap, Urbach energy and luminescence property of anatase, anatase-rutile mixed phase and of rutile phases of $TiO_2$ nanoparticles, Phys. E Low-Dimensional Syst. Nanostructures. **56**, 364–371 (2014) https://doi.org/10.1016/j.physe.2013.10.014
16. A. V. Nimmy, A. Mahesh, V. M. Anandakumar, V. Biju, Revealing the role of defect-induced trap levels in sol–gel-derived $TiO_2$ samples and the synergistic effect of a mixed phase in photocatalytic degradation of organic pollutants, Journal of Physics and Chemistry of Solids, **185**, 111774 (2024). https://doi.org/10.1016/j.jpcs.2023.111774
17. B. Choudhury, M. Dey, A. Choudhury, Shallow and deep trap emission and luminescence quenching of $TiO_2$ nanoparticles on Cu doping, Appl. Nanosci. **4**, 499–506 (2014) DOI:10.1007/s13204-013-0226-9